

# Morphological regions and oblique incidence dot formation in a model of surface sputtering

Emmanuel O. Yewande, Reiner Kree, and Alexander K. Hartmann

Institut für Theoretische Physik, Universität Göttingen,  
Friedrich-Hund Platz 1, 37077 Göttingen, Germany

(Dated: April 14, 2024)

We study solid surface morphology created by oblique-normal ion-beam sputtering with an atomistic, solid-on-solid model of sputter erosion. With respect to an earlier version of the model, we extend this model with the inclusion of lateral erosion. Using the 2-dimensional structure factor, we found an upper bound  $\gamma' < 2$ , in the lateral straggle  $\gamma$ , for clear ripple formation. Above this upper bound, for longitudinal straggle  $\gamma < 1.7$ , we found the possibility of dot formation (without sample rotation). Moreover, a temporal crossover from a hole topography to ripple topography with the same value of collision cascade parameters was found. Finally, a scaling analysis of the roughness, using the consecutive gradient approach, yields the growth exponents  $\alpha = 0.33$  and  $0.67$  for two different topographic regimes.

PACS numbers: 05.10.-a, 68.35.-p, 79.20.-m

## I. INTRODUCTION

Low energy bombardment of the surface of amorphous materials [1], semiconductors (amorphized by the sputtering process) [2, 3, 4], and metallic materials (at low temperature) [5], by a beam of ions at oblique incidence, often lead to ripple pattern formation. The ripple orientation is perpendicular to the projection of the ion beam direction, onto the surface plane, for small incidence angles, and parallel to the projection for grazing incidence. However, for a metallic surface with anisotropic diffusion, the orientation is perpendicular to a crystallographic direction (the one favored for diffusion) at small incidence angle [5].

According to the continuum theory [7, 8], ripples arise, for all angles of incidence  $\theta$ , from the curvature dependence of the sputter yield. The basis of the calculation is the Sigmund distribution [13] describing the energy deposited by the incoming ion. This distribution results from a study of the collision cascades created by the penetrating ion. The Sigmund distribution is parametrized by the depth  $a$ , the longitudinal straggle  $\gamma$ , and lateral straggle  $\gamma'$  of the energy, cf. (1). The wavelength  $\lambda_p$  obtained within the continuum theory is given by  $\lambda_p = 2 \sqrt{\frac{a}{K}} \sqrt{\frac{\gamma}{\gamma'}}$ , where  $K$  is the surface diffusivity, and  $\gamma$  is a negative surface tension coefficient, the latter depending on  $a$ ;  $\gamma$ ; and  $\gamma'$ . Typical wavelengths are of the order of tens of nanometers. In the absence of non-linearities, the dependence  $\lambda_p$  being different along the parallel and perpendicular directions to ion projection, govern the ripple orientation. However, contrary to the predictions of the continuum theory (cf. Figs. 12 and 15 of [8]), no ripples were observed in [9] for  $\theta = 40^\circ$  under Xe ion irradiation of Si.

Other studies have shown that this influence of collision cascading on topography evolution extends to quantum dot formation at  $\theta = 0$  on non-rotated substrates [10], and at  $\theta > 0$  on rotated substrates [11]. Also, collision cascade statistics has recently been found

to shift [12] the Sigmund energy distribution away from the Gaussian which has been the basis of the theoretical models so far in use [7, 14, 15]. But till now the ripple phase boundaries arising from such influence are thought to be time (i.e. influence) independent. Furthermore, up till now, dependence of ripple formation on the lateral straggle  $\gamma'$ , though acknowledged, is often ignored on accounts of isotropic or symmetric cascading for simplicity.

Recently a discrete MC model of sputter-erosion was introduced [15] which, like the continuum theories, is based on Sigmund's spatial distribution of the kinetic energy transferred by an impinging ion. Its very recent application to the study of ripple motion [16] indicates its capture of the universal features of material-surface modification by ion beam treatment, and affords us a way of exploring the different phases in the surface morphology.

In this paper, we extend this model with inclusion of lateral erosion. This includes stronger non-linearities in the sputtering process. Hence, the exponential-growth tendency of the ripple amplitude occurring within the linear theory is more stabilized [17, 18]. Furthermore, we show that the angle  $\theta_r$  above which ripple formation occurs depend on the longitudinal straggle  $\gamma$  of the ion beam, with higher  $\gamma$  resulting in lower  $\theta_r$ . Moreover, we find that there are two distinct creation mechanism for ripple: In one region of the parameter space, there is a transition from hole topography at an early time, to ripple topography at a later time. For other parameters, the ripples are created from a simple rough topography at early times. Our results also indicate the crucial role of the value of  $\gamma$  for ripple formation. If we chose  $\gamma$  larger enough, then we find dots/nano-sized islands similar to those observed by [19, 20], and predicted by [10, 11] without sample rotation. Our results suggest that by using new projectile/target combinations one might find yet unobserved surface topologies. We mention below some promising projectile/target combinations which might serve as guidelines for experimentalists.

In the next section, we describe our simulation model. In the main part we present and discuss our results. We finish with a summary and discussion.

## II. NUMERICAL SIMULATION METHODS

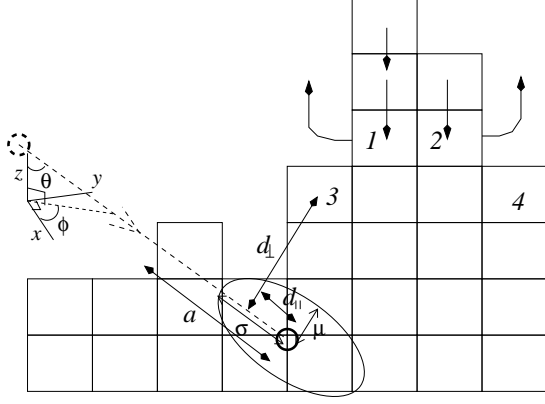


FIG. 1: Sketch showing lateral erosion of surface atom  $s$ , and collision cascade geometry, as described in the text. Erosion of atom at position 1 or 2 triggers a relaxation, which ensures there is no overhang; the atom at position 3 or 4 is only eroded, without surface relaxation.

We study system sizes  $L \times L$  with periodic boundary conditions. The material surface is defined by a time-dependent discrete height function  $h(x; y; t)$  [(2 + 1)D solid-on-solid (SOS) model] which is initially flat, i.e.,  $h(x; y; 0) = \text{constant}$ . Hence, overhangs cannot occur. We have included surface roughening via sputtering and surface smoothing via surface diffusion. Each simulation step consists of the sputtering generated by one ion and a certain number of diffusion steps. The simulation time is measured in terms of these steps and corresponds to the time in experiments. For details see Ref. [16]. Here we only display the main ingredients of the methods, for the convenience of the reader, and describe the extensions with respect to the original method.

We simulate the sputtering process as a combination of ion motion and erosion of atoms. The ion source, at some random position in a plane directly above the surface plane, projects the ions along a trajectory inclined at an angle  $\theta$  to the vertical and with azimuth  $\phi$ . After penetrating the solid through a depth  $a$ , measured along the ion trajectory, each ion comes to rest and distributes its kinetic energy  $E$ . The erosion process is governed by the generally accepted Sigmund [13] distribution. A surface atom is eroded with a probability proportional to the energy deposited there, which is given by Sigmund's formula

$$E(r) = \frac{E_0}{8} \frac{r^2}{3} \exp \left( -\frac{d_k^2}{2} - \frac{d_l^2}{2} \right); \quad (1)$$

where  $d_k = z + a$  is the distance of the surface atom, from the final stopping point of the ion, along the ion trajectory.  $d_l$  is the distance of the surface atom perpendicular to the ion trajectory. Hence, we use the local coordinate system of the ion with origin at the point of penetration, and the  $z$ -axis coinciding with the ion trajectory [15, 16]. A sketch is provided in Fig. 1. Note that all parameters depend on the experimental parameters like materials, ion energy and angle of incidence. For amorphous materials they can be estimated using the SRIM simulation package [21]. Except where otherwise stated,  $a = 6 \text{ \AA}$ ,  $E_0 = 50 \text{ eV}$ ,  $\theta = 22.5^\circ$ , and  $\phi$  is chosen to be  $(2\pi)^{1/2}$ , while, in contrast to previous studies, we vary systematically the values of  $E_0$  and  $\theta$  mimicking different material combinations.

Furthermore, we extend the sputtering model by considering lateral erosion of surface atoms; thus including non-linearity in a manner analogous to the Kardar-Parisi-Zhang (K-P-Z) non-linearity that arises from lateral attachment of adatoms in surface growth [22]. This has the effect of relaxing the surface [23] (especially as local surface slopes increase, since  $h(i+1) \neq h(i) + n_i$  where  $n_i$  is the number of surface atoms eroded in column  $i$  at that instant, due to their being closer to the stopping point of ion than topmost atom in column  $i$  (see Fig. 1)).

Surface migration is simulated [16, 24] as a nearest neighbor Monte Carlo hopping process, with a site  $i$  and nearest neighbor site  $j$  chosen randomly; and a hop  $i \rightarrow j$  allowed with probability

$$p_{i \rightarrow j} = \exp \left( -\frac{E}{k_B T} \right); \quad (2)$$

where  $E = E_S + nnE_{NN} + E_{SB}$  is an energy barrier to hopping, comprising of a substrate term  $E_S = 0.75 \text{ eV}$ , a nearest neighbor term  $E_{NN} = 0.18 \text{ eV}$  and a step barrier term  $E_{SB}$ ;  $nn$  is the number of in-plane nearest neighbors of the diffusing atom;  $T$  is the substrate temperature; and  $k_B$  is the Boltzmann's constant.  $E_{SB} = 0.15 \text{ eV}$  if there is no vacant next-nearest neighbors in the plane below the hopping atom (at site  $i$ ), and there is at least a vacant next-nearest neighbor in the plane below the hopped atom (at site  $j$ ); otherwise  $E_{SB} = 0$ . Thus this model discourages diffusion to a down-step edge but once the approach is made, it does not discourage a hop down the step (i.e. since  $E_{SB} = 0$  then; see Fig. 1 of [24]). A local heating of the surface occurs right after ion impact, followed by rapid cooling; hence surface diffusion is greatly enhanced, due to higher effective temperatures arising from the ion impacts. Consequently, we have used a higher effective temperature  $k_B T = 0.1 \text{ eV}$  in our simulations, which was estimated in our previous work [16], based on a calculation of the spatio-temporal development of the temperature, arising from the local heating [25] (see also [26]).

### III. RESULTS AND DISCUSSION

The profiles shown in the figures are from sizes  $L^2 = 128^2$ , and the bar, on the profiles, indicate the ion beam direction. Distances are in units of a lattice constant, and time in ions/atom; except where stated otherwise. By varying the collision cascade parameters  $\alpha$  and  $\beta$ , we explore the full topographic features of this sputter-erosion model, for typical ion energies on the order of 1K eV; keeping  $\alpha$  and  $\beta$  constant.

We start with a sketch (Fig. 2) of the six topographic regions that were found, corresponding to different combinations of  $\alpha$  and  $\beta$ , for  $t = 3$  ions/surface atom at which almost all the surface topographic features are distinct; the corresponding profiles are shown in Fig. 3. Note that the boundaries shown in this sketch do not represent abrupt transitions from one topography to another, as we shall see below (in Figs. 11, 10). Rather we observe often a smooth crossover from one behavior to the other. Note that the system is still not in (dynamic) equilibrium [15], hence the surface morphology still evolves with time and at later time a diagram of the type of Fig. 2 will look different. We have picked a typical time, corresponding to tin scales easily accessible in experiments, which exhibit a rich behavior as a function of the straggling parameters  $\alpha$  and  $\beta$ . Also, although the sketch is specially at  $\theta = 50^\circ$ , similar "phases" also occur at other values of  $\theta$ , with slight deviations at the boundaries. Examples of a few experimental parameters (ion energy, type of material, type of ion etc.) which lead to the specific parameters used here we obtained from a SRIM simulation [21], are; region V: 1.5–1.7K eV neon (Ne)-ion, or 2.25–2.5K eV argon (Ar)-ion, sputtering of copper (Cu), or silver (Ag); 1.2–1.4K eV Ne-ion, or 1.7–2.0K eV Ar-ion, sputtering of germanium (Ge), or gallium arsenide (GaAs); 170–200eV helium (He)-ion sputtering of graphite (C); region IV: 650–800eV Ne-ion sputtering of silicon (Si); region III: 800eV–1.1K eV Ar-ion sputtering of silicon (Si); 550–700eV Ne-ion sputtering of C; with fluences  $10^{14}$ – $10^{15}$  ions/cm<sup>2</sup>. Note that for most materials and parameter combinations, hence the region VI might be difficult to access. Also, SRIM simulations reveal that very large  $\alpha$  and  $\beta$ , i.e., beyond the values considered here, are impractical, since they can only occur for a higher  $a$ . But the value of  $a$  is itself restricted by the range of ion energies that lead to ripple formation. We are not aware of an experimental study of the sputtering behavior where the parameters are varied systematically in the  $\alpha$ - $\beta$  plane. Hence, when using these parameters in experiments, one might be able to observe the topographies of Fig. 3, where some of them have not been observed so far.

A brief description of each topographic region in Fig. 3, including the behavior at later times  $t = 3$  (atoms/surface atom), is as follows: Region I: rough surface [see Fig. 3(a)] which, as time increases, evolves to a hole topography. The sizes of the holes grow and finally coalesce to a ripple topography at long times (Fig. 4).

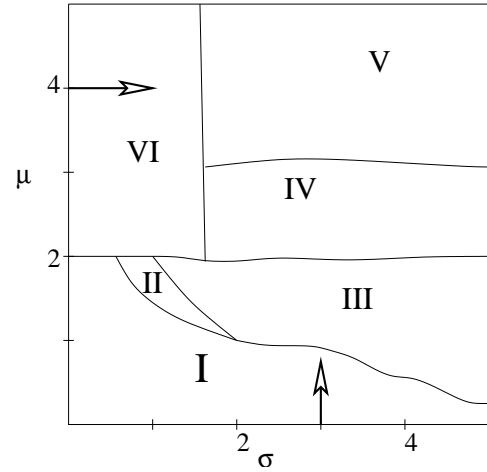


FIG. 2: Different topographic regions ( $\theta = 50^\circ$ ,  $a = 6$ ). Region I: rough surface; II: holes; III: clear ripples oriented perpendicular to ion beam direction; IV: short ripples (resulting from increased  $\mu$ ); V: dots; VI: non-oriented structures. The arrows indicate the directions referred to in Fig. 8.

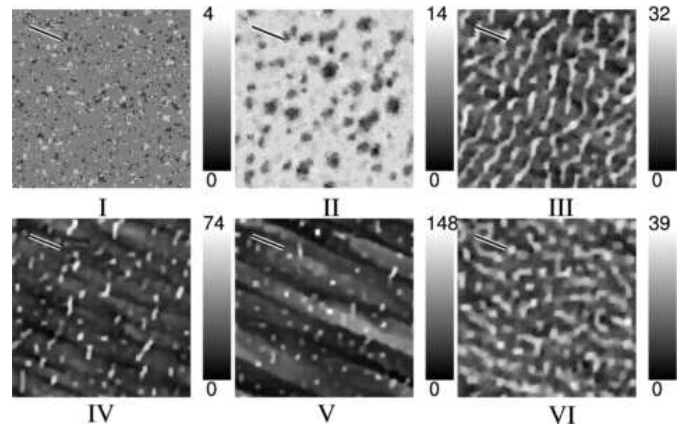


FIG. 3: Profiles for parameters chosen from each topographic region in Fig. 2;  $\theta = 50^\circ$ ,  $a = 6$ ,  $t = 3.0$ . (I)  $\alpha = 1$ ,  $\beta = 0.5$ ; (II)  $\alpha = 1$ ,  $\beta = 1.5$ ; (III)  $\alpha = 3$ ,  $\beta = 1.5$ ; (IV)  $\alpha = 4$ ,  $\beta = 2.5$ ; (V)  $\alpha = 5$ ,  $\beta = 5$ ; (VI)  $\alpha = 0.5$ ,  $\beta = 5$

Region II: holes are already prominent in this region [see Fig. 3(b)]; Here the number of holes in this region increases with time, and again ripples are formed at long times, but at an earlier time than as in region I (not shown as separate figure).

The number of holes decreases when increasing the sputterin depth  $a$  [Fig. 5 (a)–(c)]. The number of holes also decreases with decreasing  $\beta$  [Fig. 5 (d)–(f)], while ripples are formed already at this early time in this region if  $\alpha$  is increased beyond  $\alpha_c(t = 3) \approx 60^\circ$ .

Region III: the ripple phase [15, 16]. Having observed in regions I and II that holes evolve into ripples with time, we studied this region from the very earliest times ( $t = 0$ –3) but found only very tiny holes, i.e. not as pronounced as

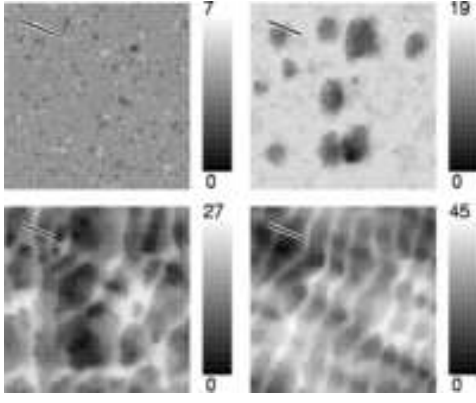


FIG. 4: Surface profiles of region I,  $\theta = 1^\circ$ ,  $\phi = 1^\circ$ . From top-bottom, left-right,  $t = 3, 20, 40$ , and  $90$ .

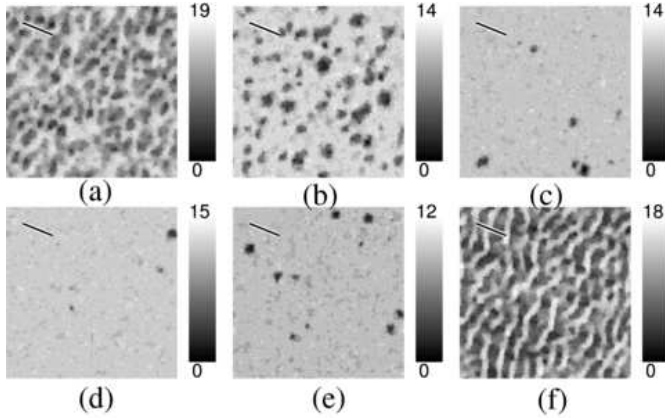


FIG. 5: Surface profiles of region II,  $t = 3$  ions/atom ( $\theta = 1^\circ$ ,  $\phi = 1.5^\circ$ ). Top row;  $\theta = 50^\circ$ ,  $a = 5$  (a),  $a = 6$  (b), and  $a = 7$  (c). Bottom row;  $a = 6$ ,  $\theta = 40^\circ$  (d),  $45^\circ$  (e), and  $60^\circ$  (f).

in region II, in the course of ripple formation, see Fig. 6).  $\theta \approx 30^\circ$  in this region. This means, comparing regions I, II and three, there seem to be two different processes of ripple formation. Ripples can be formed quickly by evolving directly from a slightly rough surface, or they can be formed slowly via the creation of holes, which coalesce to ripples on longer time scales. Note that in regions I, II, the resulting ripple wavelength is smaller than the size of the holes generated on smaller time, while in region III the ripple wavelength is larger than the tiny holes.

We also studied here the case of smaller angles, e.g.  $\theta = 30^\circ$ , see Fig. 7. Hence, for lower angles of incidence, ripple formation is shifted to later times, but the ripples tendency again increases when increasing the longitudinal struggle. This indicates that there might be a lower critical angle  $\theta_c$ , below which no ripple formation happens even at long times. Such an effect has been observed in experiments [9] of sputtering  $\text{Xe}^+$  on Si, where below  $\theta_c = 40^\circ$  no ripples have been found at finite but

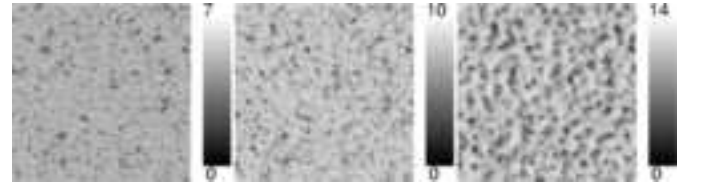


FIG. 6: Surface profiles of region III, at very early times. From left-right,  $t = 0.1, 0.2$  and  $0.5$  ions/atom ( $\theta = 3^\circ$ ,  $\phi = 1.5^\circ$ ,  $\theta = 50^\circ$ ,  $a = 6$ ).

long ion fluences. For even smaller angles like  $\theta = 20^\circ$ , we indeed do not observe ripple formation within the time scales (i.e. fluences) we can reach in our simulations. Note that a general statement about the existence of such a critical angle  $\theta_c(\phi)$  would require simulations up to very large times for all parameters studied here, which is beyond the numerical capacities. Hence, we remain with the statement that our numerical results indicate that such critical angles indeed exist, without the possibility to determine them precisely.

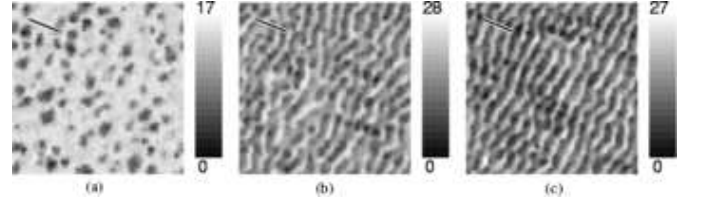


FIG. 7:  $\theta = 30^\circ$ ,  $a = 6$ ,  $\phi = 1.5^\circ$ ;  $\phi = 2$  (a);  $\phi = 3$  (b); and  $\phi = 5$  (c).

Region IV: consists of a mixture of dots and short ripples, which eventually give way to the dot "phase" (region V), as  $\theta$  is increased. Hence, this region seems to "interpolate" between regions III and V.

Region V: consists of dots. These dots are formed on some ripple-like structures oriented perpendicular to the ion beam direction, as discussed below with more detail. Noting that our model is a solid on solid model on a square lattice, the dots are not unsimilar to the QDs predicted by theory [10, 11] and observed in experiments [6, 20].

Region VI: consists of non-oriented structures exhibiting a typical lengthscale, but only a slight orientational preference parallel to the ion beam. This region, as mentioned above, is probably difficult to access in experiments.

A closer look at the dot profiles of region V in Fig. 3 reveals the presence of some underlying large-scale structures. We now discuss this region and its adjacent regions III and V with more detail. The underlying structure is clearly seen in a 2D structure factor,  $S(k) = \langle h(k)h(-k) \rangle$ , where  $h(k)$ , the Fourier transform of the height profile  $h(x)$ , with mean  $\langle h \rangle = \int_{-L}^L h(x) dx = L^2$ ,

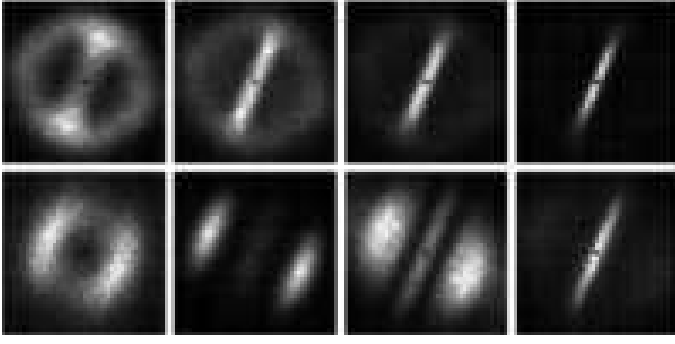


FIG. 8: 2D structure factor ( $L=128$ ). Top, along  $\alpha = 4$  in Fig. 2, left-right:  $k_{\parallel} = 0.5, 1.0, 1.5$ , and  $3.0$ . Bottom, along  $\alpha = 3$ , left-right:  $k_{\parallel} = 0.5, 1.0, 1.5$ , and  $3.0$

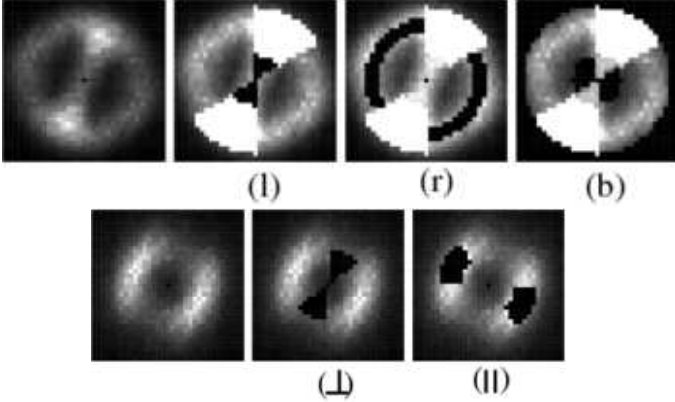


FIG. 9: Separation of the 2D  $S(k)$  (first image top and bottom) into regions (in black from second image), for the purpose of our analysis. The letters l, r, b, denote line, ring and background, respectively; and the symbols,  $\perp$  and  $\parallel$ , denote the perpendicular and parallel directions, respectively; as referred to in the text. The white regions are excluded from the analysis.

at time  $t$ , is given by

$$h(k) = \frac{1}{L} \sum_r [h(r) - \bar{h}] \exp(ik \cdot r); \quad (3)$$

The 2D structure factor shown in Fig. 8 has been obtained from an average of 600 independent runs, for parameter along  $\alpha = 4$  (top row), and along  $\alpha = 3.0$  (bottom row). In these diagrams the structure factor for the  $k$ -vector  $(k_x; k_y) = (0; 0)$  is displayed in the center and the corners represent the values for  $(k_x; k_y) = 2$  ( $1=8; 1=8$ ). The case of  $\alpha = 4.0$ , when moving from small values of  $k_{\parallel}$  to larger values (i.e. left-right in Fig. 2) is shown in the top row of Fig. 8. For small values of  $k_{\parallel}$ , we are in region IV, where we see a typical wavelength, but almost no orientation. This translates to a ring visible in the  $S(k)$  plot. Note that there is a slight preference for an orientation parallel to the ion beam, being visible via two peaks in  $S(k)$  at wave vectors perpendicular to

the ion beam. When increasing  $k_{\parallel}$ , one moves into region V. Here a line perpendicular to the ion beam emerges in the structure factor rather abruptly around  $k_{\parallel} = 1$ . This line represents the underlying structures parallel to the ion beam, being visible in Fig. 2. Note that the "dots" emerge on top of these structures; in the 2D structure factor their signal is too weak to be visible.

On the other hand, along  $\alpha = 3.0$ , we initially see (bottom line from bottom-left Fig. 3) an orientation, spread around ion beam direction (for instance, at  $k_{\parallel} = 1.0$ ), with a more restricted range of  $k$  which is typical of the thin wobbly ripples. As  $k_{\parallel}$  increases, we move to the region V as discussed above, but we do not observe an abrupt change, because for a large range of values of  $k_{\parallel}$ , ripples, dots and the underlying parallel structures coexists (region III).

To study the crossover or transition from one region to the other in a quantitative way, it might be more instructive to look at order parameters which are numbers rather than the full 2D structure factor. We first define a quantity  $Q = S^{\parallel}(k_{\parallel})/S^{\perp}(k_{\perp})$ , where  $S^{\parallel}(k_{\parallel})$  is the maximum, for  $k$  parallel (perpendicular) to ion beam direction. This quantity detects the change of orientational order.

When moving along  $\alpha = 4$  from region VI into region V we expect a rather abrupt change of the behavior from the visual inspection of the 2D structure factor (top row of 8). The behavior of  $Q$  when changing  $k_{\parallel}$  for  $\alpha = 4$  is displayed in the inset of Fig. 10. For small values of  $k_{\parallel}$ , i.e. in region VI, there is only a slight preference of structures parallel to the ion beam (corresponding to  $k_{\parallel}$ ) which leads to small values  $Q \approx 2$ . When going beyond  $k_{\parallel} = 1$ , i.e. when moving into region V, the domination of the longitudinal structures increases, leading to a growth of  $Q$ .

We furthermore want to go beyond studying the height of peaks of  $S(k)$  by examining the presence or absence of a typical length scale in the system. This length scale is visible in the 2D structure factor via bright spots (oriented) or a bright ring. For this purpose, we also look at the relative weights

$$q_{k=y} = \frac{\int_{A_x} S(k) da}{\int_{A_y} S(k) da}; \quad (4)$$

of certain areas in the 2D structure factor, where the integration  $da$  extends over areas  $A_x = A_y$  of  $k$ -points. The indices  $x; y = l; r; b$ , refer to  $k$  values on the line, ring and background (outside line and ring) respectively, as shown in the upper part of Fig. 9. The white regions, in this figure, are excluded from our analysis, because they contain a superposition of  $k$ s on both the line, and the ring. A plot for  $q_{k=b}$  is shown in Fig. 10, other combinations (not shown) yield results with information not going beyond the study of  $Q$ . For  $q_{k=b}$  we observe an abrupt change around  $k_{\parallel} = 1$  with the ring becoming almost indistinguishable ( $q_{k=b} \approx 1$ ) from the background for  $k_{\parallel} > 1.5$ , signaling the disappearance of a typical

length scale around  $\mu = 1$ . Note that  $q_{\Gamma=b}$  stays almost constant for the full region V, in contrast to the behavior of  $Q$ .

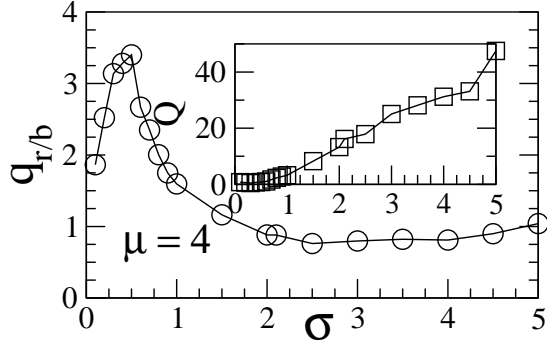


FIG. 10: Plot of the quantities  $q_{\Gamma=b}$  and  $Q$  (inset) as a function of  $\mu$ , along  $\sigma = 4.0$ , as described in the text.

Now we turn to the behavior along the  $\sigma = 3$  line, i.e. when moving from region I, into region III, then IV and finally V. The behavior of  $Q$  as function of  $\mu$  (bottom row of Fig. 8) is displayed in the inset of Fig. 11. The crossover around  $\mu \approx 2$  from the ripple region (II) where  $k_k$  wave vectors dominate ( $Q < 1$ ) to the region V where  $k_{\parallel}$ -structures dominate is clearly visible.

The same result is obtained, when again studying not only peaks, but integrated structure factors over certain selected areas. Hence, we also study  $k$ -vectors parallel and perpendicular to the ion beam ( $x; y = k; ?$ ), as shown in the lower part of Fig. 9. Also  $q_{\Gamma=k}$  exhibits a strong growth for  $\mu > 2$ , i.e. when moving into region III.

Finally, a study of  $q_{\Gamma=b}$  (not shown) again confirms the loss of a certain length scale when moving into region V. This is again visible via the disappearance of weight on the ring in the 2D structure factor with respect to the background [see again Fig. 8]. In any case, we have

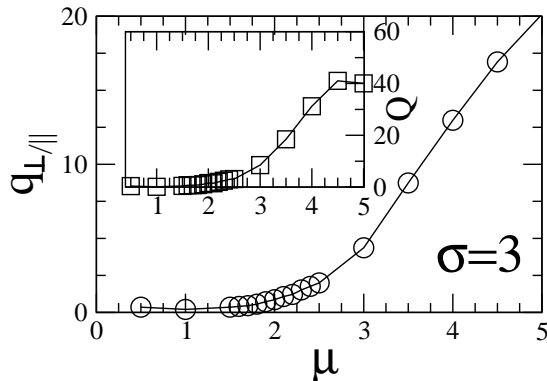


FIG. 11: Plot of the quantities  $q_{\Gamma=k}$  and  $Q$  (inset) as a function of  $\mu$ , along  $\sigma = 3.0$ , as described in the text.

mainly looked at snapshots at time  $t = 3$ , corresponding to typical experimental fluences of  $10^{15}$  ions/cm<sup>2</sup> (as

already stated above). Hence, the location of the exact boundaries between the different regions, is not a major interest here. We only want to demonstrate, that indeed order-parameter-like functions can be defined. The full information is anyway contained in the 2D structure factors.

In the asymptotic limit, the morphology of sputtered surfaces may be described by the noisy Kuramoto Sivashinsky equation [14]

$$\partial_t h = -\kappa \partial_x^2 h + \gamma \partial_y^2 h + \frac{\kappa}{2} (\partial_x h)^2 + \frac{\gamma}{2} (\partial_y h)^2 - K \partial^4 h + \xi; \quad (5)$$

where  $\kappa(\gamma)$ ,  $\gamma(\gamma)$ , is the effective surface tension coefficient, and nonlinear coefficient, respectively, along a direction parallel (perpendicular) to the projection of the ion beam direction onto the surface plane (here, the  $x$ -axis is parallel to the projection);  $K$  is the surface diffusion constant; and  $\xi$  is an uncorrelated white noise with zero mean. These coefficients are explicitly given, in terms of the sputtering parameters, in ref. [8]. Note that erosion of surface material tends to maximize the exposed area, so-called negative surface tension, hence, for the sputtering phenomena, this instability constrains the coefficients  $\kappa$  and  $\gamma$  to be negative.

At early times, the local slopes are small enough in most of the regions for us to ignore the nonlinearities; we are therefore left with a noisy Bradley-Harper equation [7]. A plot of the coefficients for our parameter range, along  $\sigma = 3$ , is shown in Fig. 12;  $\gamma_k$  and  $\gamma_{\parallel}$  are nonzero always which implies the presence of two length scales. Hence, according to the linear continuum theory, ripples parallel and perpendicular to the ion beam direction are always present in the system; the one observed is the one for which  $\gamma_{\parallel}$  is highest; i.e. with the highest amplitude-growth rate  $R = (\kappa k_k^2 + \gamma k_{\parallel}^2) - K(k_k^2 + k_{\parallel}^2)^2$  [7].

We now try to understand roughly the behavior along the above discussed  $\sigma = 3$  and  $\sigma = 4$  lines within the linear theory. For a full understanding one would have to consider also the nonlinear terms, where the full dependence on the parameters is yet not available to the authors. In Fig. 12 the values of  $\kappa$  and  $\gamma$  are shown as function of  $\mu$  (main plot) and  $\mu$  (inset) along these lines. For the case  $\sigma = 4$  (see inset), we observe that  $\kappa > 0$  for all values of  $\mu$ , hence the preferential orientation is always parallel to the ion beam, as observed. To understand the crossover from region VI to region V, one has probably to consider the nonlinear terms.

For the  $\sigma = 3$  line, we observe  $\gamma_{\parallel} > \gamma_k$  for  $\mu < 1$ , which is compatible with the behavior in region I, where no preferential orientation is observed. For  $1 < \mu < 2.5$ ,  $\gamma_k > \gamma_{\parallel}$  which implies the dominance of ripples with  $k_k$  (i.e. with wavelength  $\lambda = 2\pi / k_k$ ), as we have seen in region III and partly in the crossover region IV. In region IV ripples are still present, but dominate less. For  $\mu$  above this range, the structures with  $k_{\parallel}$  dominate. However, the positive value of  $\kappa$  for higher  $\mu$  is contrary to our results, since it implies a preferential smoothing

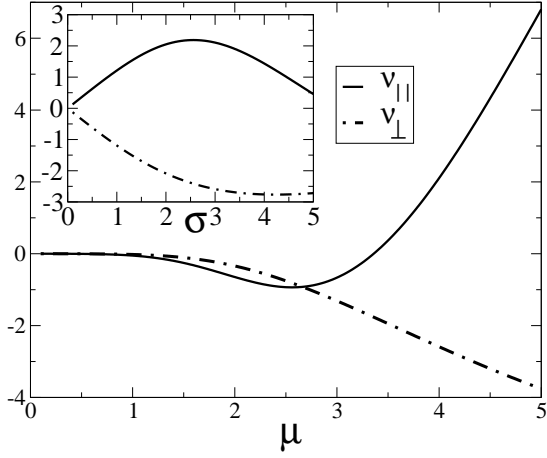


FIG. 12: The surface tension coefficients of Eq. 5, along  $\sigma = 3.0$ , for our simulation parameters.  $\beta = 50^\circ$ ,  $a = 6.0$

along the parallel direction. We have not observed such smoothening, here probably nonlinear effects are more important. If we consider the maximum of  $j_k j$  and  $j_z j$  for the region where  $k < 0$  and/or  $p_{\text{exp}} < 0$ , then we see that this maximum is obtained in region V for large  $\mu$ . Indeed we observe that region V is rougher than e.g. region III, see below.

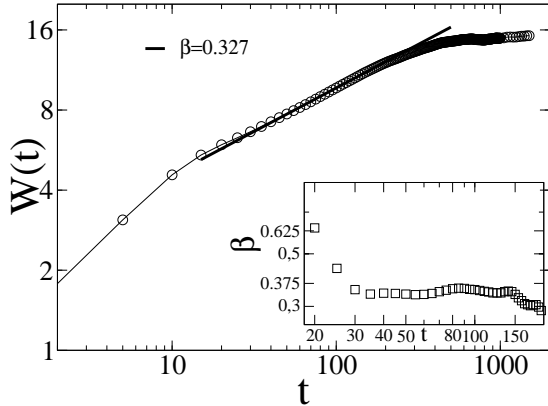


FIG. 13: Surface width  $W$  versus time,  $\beta = 3$ ,  $\beta = 1.5$  (region III),  $\beta = 50^\circ$ . In the inset is a plot of the consecutive slopes for  $t = 20 \dots 200$ , where the lower and upper cut-offs are seen to occur at  $t = 35$  and  $150$  respectively.

But, before we proceed, we should recall that regions I and II eventually evolve to a similar ripple topography as in region III; region IV is an intermediate stage and VI is hardly experimentally accessible. Therefore, we are interested in two different scaling regions, i.e., arising from ripple-yielding, as well as dot yielding parameters. We use the finite-size scaling behavior of the surface width/roughness,

$$W(L; t) = L f\left(\frac{t}{L^z}\right); \quad (6)$$

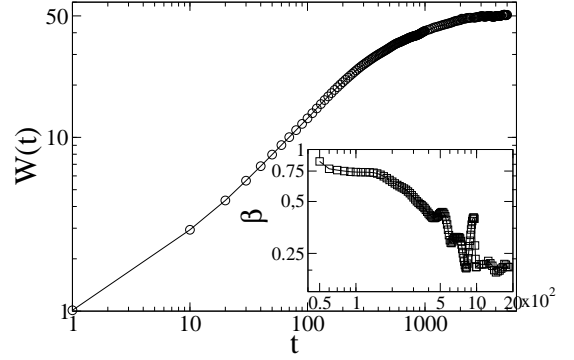


FIG. 14: Surface width  $W$  versus time,  $\beta = 5$ ,  $\beta = 5$  (region V),  $\beta = 50^\circ$ . In the inset, time is in multiples of  $10^2$ ; there are two scaling regions  $t = 40 \dots 140$  and  $t = 1000 \dots 1800$ , which yields  $\beta = 0.665$  and  $0.137$  respectively.

where  $\beta$  and  $\beta_z$  are the roughness exponent and growth exponent, respectively; and  $W = \sqrt{\langle (h(r) - \bar{h})^2 \rangle} = L^z$ , i.e.,  $W$  is the root-mean-squared fluctuations in the surface height. (6) defines two scaling regions, separated at the saturation time  $t_s(L) / L^z$ .  $z = \beta$  is the dynamic exponent. In the first region ( $t < L^z$ )  $W / t^\beta$ , independent of  $L$ ; and in the second region ( $t > L^z$ )  $W / L^\beta$ , constant in time [27]. A scaling argument in [18] reveals that  $t_s$  increases with the diffusion coefficient, and with decreasing strength of non-linearities [28].

In the following roughness analysis, we rescale the time unit such that  $L^2$  particles are eroded in unit time, which is analogous to the measure of time in simulations of epitaxial growth on vicinal surfaces.

We obtained our scaling exponents from an average of 600 independent runs. Fig. 13 is a plot of the surface width  $W(t)$  for  $L = 128$ , we determine the actual scaling region of  $\beta$  from the consecutive slopes [27] of  $W(t)$  for  $t < L^z$ ; shown in the inset of Figs. 13 and 14 where a  $t$  to this region gives  $\beta = 0.327 \pm 0.001$  and  $\beta = 0.665 \pm 0.003$  (from the scaling for times around  $t = 100$ ) for the topographic regions (see Fig. 2) III and V respectively.

Our exponents are quite different from the scaling of the KPZ equation [22] in  $(2+1)$  dimensions [27, 29], which shows that for these parameter choices, either one or both of the negative surface tension coefficients, in the noisy KS equation [14], do not renormalize to positive values. That is, if indeed, this atomistic model which is known to accurately describe the morphology of sputtered surfaces at early and long times [15, 16, 30], can be represented by the noisy KS equation, in the asymptotic limit, as expected for the sputtering phenomenon.

#### IV. CONCLUSIONS

We have extended the study of surface topography induced by ion bombardment beyond the circular-symmetric collision cascade case  $\beta = \beta_z = 1$ ; using a

discrete Monte Carlo model. We found an upper bound  $\gamma' > 2$  for clear ripple formation. We observed a crossover from hole topography to ripple topography, for same collision cascade parameters. Above the upper bound we found a crossover to a dot topography; our results indicate the non-trivial influence of the value of  $\gamma$  for the surface topography. Moreover, we found the possibility of dot formation for  $\gamma > 2$  and  $\alpha < 1.7$ , without sample rotation.

Also, we found the possibility of different incidence  $\gamma_r$ , around which ripple formation is possible, as in the experiment; our results indicating that high value of the longitudinal straggling result in lower value of  $\gamma_r$ . Finally, we found that the collision cascade parameters affect the growth exponent.

Our results indicate that using new target/projectile combinations different in experiments might lead to surface topographies yet not observed. Here a systematic study covering the full parameter space (at least in the range ( )) would be very interesting, which has not

been done so far to our knowledge. Furthermore, it would be nice to investigate the small-time behavior, i.e. the ripple formation process, experimentally. In this way one could verify whether the two different creation mechanisms we have observed, hole-coalescence and creation from a rough surface, can be observed in experimental systems.

#### Acknowledgments

The large scale numerical simulations were performed on the workstation clusters of the institute. This work was funded by the DFG (Deutsche Forschungsgemeinschaft) within the SFB (Sonderforschungsbereich) 602: Complex Structures in Condensed Matter from Atomic to Mesoscopic Scales and by the Volkswagen-Stiftung (Germany) within the program "Nachwuchsgruppen an Universitäten".

- 
- [1] T. M. Mayer, E. Chason, and A. J. Howard, *J. Appl. Phys.* 76, 1633 (1994).
  - [2] E. Chason, T. M. Mayer, B. K. Kelerman, D. T. M. CIlroy, and A. J. Howard, *Phys. Rev. Lett.* 72, 3040 (1994).
  - [3] J. Erlebacher, M. J. Aziz, E. Chason, M. B. Sinclair, and J. A. Florio, *Phys. Rev. Lett.* 82, 2330 (1999).
  - [4] S. Habenicht, K. P. Lieb, J. Koch, and A. D. Wieck, *Phys. Rev. B* 65, 115327 (2002).
  - [5] S. Rusponi, G. Costantini, C. Boragno, and U. Valbusa, *Phys. Rev. Lett.* 81, 2735 (1998).
  - [6] R. Gago, L. Vazquez, R. Cuerno, M. Varela, C. Ballesteros, and J. M. A. Bella, *Appl. Phys. Lett.* 78, 3316 (2001).
  - [7] R. M. Bradley and J. M. E. Harper, *J. Vac. Sci. Technol. A* 6, 2390, (1988); and references therein.
  - [8] M. M. Makeev, R. Cuerno and A. -L. Barabasi, *Nuc. Instr. and Meth. in Phys. Res. B* 197, 185 (2002).
  - [9] G. Carter, and V. V. Ishnyakov, *Phys. Rev. B* 54, 17647 (1996).
  - [10] B. Kahng, H. Jeong, and A. -L. Barabasi, *Appl. Phys. Lett.* 78, 805 (2001).
  - [11] F. Frost, *Appl. Phys. A* 74, 131 (2002).
  - [12] M. Feix, A. Hartmann, R. Kree, J. Muñoz-García, and R. Cuerno, *Phys. Rev. B* 71, 125407 (2005).
  - [13] P. Sigmund, *Phys. Rev.* 184, 383 (1969).
  - [14] R. Cuerno and A. -L. Barabasi, *Phys. Rev. Lett.* 74, 4746 (1995).
  - [15] A. K. Hartmann, R. Kree, U. Geyer, and M. Kolbel, *Phys. Rev. B* 65, 193403 (2002).
  - [16] E. O. Yewande, A. K. Hartmann, and R. Kree, *Phys. Rev. B* 71, 195405 (2005).
  - [17] M. Rost and J. Krug, *Phys. Rev. Lett.* 75, 3894 (1995).
  - [18] S. Park, B. Kahng, H. Jeong, and A. -L. Barabasi, *Phys. Rev. Lett.* 83, 3486 (1999).
  - [19] F. Frost, A. Schindler, and F. Bigl, *Phys. Rev. Lett.* 85, 4116 (2000).
  - [20] S. Facsko, T. Dekorsy, C. Koerdt, C. Trappe, H. Kurz, A. Vogt, and H. L. Hartnagel, *Science* 285, 1551 (1999).
  - [21] J. F. Ziegeler, J. P. Biersack and K. Littmark, *The Stopping and Range of Ions in Matter*, (Pergamon, New York 1985); see also <http://www.srim.org/>.
  - [22] M. Kardar, G. Parisi, and Y. -C. Zhang, *Phys. Rev. Lett.* 56, 889 (1986).
  - [23] E. O. Yewande, unpublished.
  - [24] P. Smilauer, M. R. Wilby, and D. D. Vvedensky, *Phys. Rev. B* 47, 4119 (1993).
  - [25] N. A. Marks, *Phys. Rev. B* 56, 2441 (1997).
  - [26] J. Melngailis, *J. Vac. Sci. Technol. B* 5, 469 (1987).
  - [27] A. -L. Barabasi and H. E. Stanley, *Fractal Concepts in Surface Growth* (Cambridge University Press, Cambridge, 1995).
  - [28] See also: Z.-W. Lai and S. Das Sarma, *Phys. Rev. Lett.* 66, 2348 (1991); where another non-linearity, distinct from the KPZ non-linearity was shown to affect the surface topography, in conserved MBE, in a similar manner.
  - [29] J. G. Amar and F. Family, *Phys. Rev. A* 41, 3399 (1990).
  - [30] A. D. Brown, J. Erlebacher, W. -L. Chan, and E. Chason, *Phys. Rev. Lett.* 95, 056101 (2005).